ADVANCED OPTICAL MATERIALS

Supporting Information

for *Advanced Optical Materials,* DOI: 10.1002/adom.201700195

Experimental Route to Scanning Probe Hot Electron Nanoscopy (HENs) Applied to 2D Material

*Andrea Giugni, Bruno Torre, Marco Allione, Gobind Das, Zhenwei Wang, Xin He, Husam N. Alshareef, and Enzo Di Fabrizio**

Supporting Information

Experimental route to scanning probe hot electron nanoscopy (HENs) applied to 2D material.

*Andrea Giugni, Bruno Torre, Marco Allione, Gobind Das, Zhenwei Wang, Xin He, Husam N. Alshareef, and Enzo Di Fabrizio**

Andrea Giugni[1], Bruno Torre[1], Marco Allione[1], Gobind Das[1], Zhenwei Wang[2], Xin He[2], Husam N. Alshareef[2] and Enzo Di Fabrizio[1]

[1] King Abdullah University of Science and Technology (KAUST), Physical Sciences and Engineering Division (PSE), Thuwal 23955-6900, Saudi Arabia.

[2] King Abdullah University of Science and Technology (KAUST), Materials Science and Engineering Division (MSE), Thuwal 23955-6900, Saudi Arabia.

*Corresponding author: enzo.difabrizio@kaust.edu.sa

TOC:

Figures. S1 to S12

References (1-9)

Materials and Methods

The device investigated in the paper *"Experimental route to scanning probe hot electron nanoscopy (HEN) applied to 2D material"* consists of a van der Walls (vdW) n-p heterojunction,[1] extending for about 30x5 microns. It is realized with the use of a 2D-layered transition-metal dichalcogenide of MoS_2 (7 layers), with n-type character, and a p-type semiconductor realized by a tin monoxide (SnO) sputtered layer, about 14 nm high.

This seven layers vdW junction has been demonstrated to be a competitive 2D diode with a rectification ratio up to $5*10^2$ at the macro scale with the possibility to be used as a gate-tunable diode.[2] Here we used a plasmonic device with nanometric apex combined with a metallized grating coupler, realized upon an AFM tip, to probe the local nanoscale electronic conduction properties of the junction in the dark and under illumination. Current characteristic is typical of those of point contact junctions with vdW interaction forces between the contact interfaces, this revealed by the barrier lowering and apparent gap reduction, with a current signal amplitude depending on the control force used to push the tip on the surface of the 2D junction. With the use of the scanning nano-tip it was investigated the two fundamental interface geometries at the contact of a 3D material with the 2D MoS_2 layered crystal, revealing the large conductance anisotropy. Synchronous lock-in detection allowed to discriminate photo-generated hot charges from those due to the polarization of the device.

The fabrication of the plasmonic tip was done by combining induced electron beam deposition at 5 KeV energy, by using Pt-based precursor gas, for the cone growth and focused Ga ion milling technique, at 30 KeV, to realize the coupler grating. At the end, the device was covered by 90 nm Gold-sputtered with a procedure that maintains the tip apex radius in the range of few tens of nanometers. The grating, acting as unidirectional SPPs launcher, allows the conversion of free propagating laser beam into surface plasmons. Coupled SPPs move along the tapered guiding structure, promoting the concentration of energy at its apex where SPPs damp out as photons and hot

electrons. Hot charges with enough energy, cross the Schottky barrier flowing directly in the semiconductor regardless the depletion contact extension. Far field excitation, taking advantage from the propagation-induced SPP focusing, allows for spatially separated SPPs coupling and probe apex excitation with high S/N ratio.

S1. Numerical simulation for the optimal coupler.

Here, the purpose of our simulations is to analyze the laser coupling efficiency into a propagating plasmonic mode by using a grating realized on one side of a commercial AFM cantilever tip.

AFM probes have side surface areas of tens of micron squares with a height from the lever base to the tip of about 10 microns. These characteristics allow for the realization of a grating coupler directly on one or more of the tip side-faces and, accordingly to tip shape and the scattering geometry adopted, it can accommodate up to tens of grooves. The simulations show a remarkable effect on the coupling efficiency of the far-field laser beam on the generation of bound SPPs.

The period of the grating depends on the beam wavelength, coupling angle, and the surface waves effective index n_{eff}. The power profile along the grating and the incident angle, indicated as $\alpha(z)$ and θ_{in} in eq.1 of the main text, determine the optimal size of the incoming beam for the maximal coupling efficiency.

Power coupling profile is the main factor in the beam coupling and is different if a plane wave or a Gaussian beam profile is used in the optimization procedure.[3] Matching the dissipative SPP losses along the grating with the coupling strength allows maximizing the coupling efficiency. From the optical point of view, this is the most relevant difference between a SPP launcher and a photon diffraction grating.

In the electromagnetic simulations presented, we have represented the real 3D scenario with a 2D model. This representation allowed a sensible reduction of the simulation time against an acceptable increase of the uncertainty in the efficiency determination. These uncertainties reflect the

approximations due to the reduction to the same symmetry of the axial-symmetric Gaussian beam and the 1D translational symmetry of the linear grating.

The scattering of freely propagating photons in SPPs requires the fulfillment of the energy and momentum conservation rules in the interaction process that fixes the frequency and determines the amount of momentum needed accordingly to the dispersion relations of the two bosons, eq.1 in the main text.

In the numerical simulations we have made use of a commercial FDTD package (FDTD Solutions, Lumerical Inc.). The simulations have been performed in 2D by considering a 1D TM polarized focused Gaussian beam profile having a waist width of 4 μm FWHM and an incident angle of θ_{in} = -6.7° on the surface normal.

The illumination geometry was chosen to reproduce the experimental set up (See setup description paragraph below). This means we have considered an AFM tip declination angle of 11°, a nose cantilever type from Atec, and a focused beam propagation at nearly grazing conditions with respect to the sample surface, with an optical axis elevated 10° on the horizontal sample plane. In this configuration, the specular reflection of the incoming beam propagates away from the sample resulting in an increased S/N ratio of any spectroscopic application.

The beam was assumed to be launched 2 μm above the structure while its offset with respect to the grating firing edge has been considered one of the free parameters for the optimization of the generation of SPPs propagating in the -z (grating) direction.

The figure of merit considered is the launching efficiency of the SPPs at a defined wavelength into the desired propagation direction. The efficiency has been measured through a series of power monitors set at 10, 5, and 2 microns from the grating. We evaluated the SPP propagation length, about 12 μm at 633 nm for gold material, and extrapolated the efficiency

value at z = 0, the coordinate coincident with the grating firing end, as reported in Figure 1a of the main text.

In this scattering geometry, a uniform plasmonic grating launcher can reach a unidirectional efficiency up to 40%, as reported in Figure S3a. Figure S3 compare the results for the uniform grating with those obtained introducing a linear variation of the pitch and of the duty cycle, and with a coupler constituted by isolated wires. Moving from the uniform grating to the wires the main differences, apart from the maximal efficiency obtained, are that the shape changes reducing the gap between the wires and increasing sensibly the depth of the groves more than a factor 4. A complete discussion of these interesting result will follows in a dedicate publication.

We considered for the simulations a variable step mesh with the finest mesh step near the interfaces down to 3 nm and matching each groove surface, see Figure S1a. In this way, the refractive index edges were optimally defined along the structure directions for each simulated configuration. Furthermore, each grooves edge has been rounded with a radius of curvature of 20 nm, mimicking a typical experimental case (Figure S1b). The electromagnetic simulation starts with the launch of an electromagnetic pulse of predefined spectral and spatial shape (Figure S1c, S1d) and then proceed evaluating the evolution in time of the electromagnetic field in the simulation box. The simulation is continued in time until the amplitude of any component of the field in any part of the box becomes negligible. This allows to follow temporarily the pulse (Figure S1e S1f), to evaluate the electric field components along specific directions (Figure S1g), or to measure the total power flowing across monitors (Figure S2a S2e) as a function of several parameters, such as for example the wavelength.

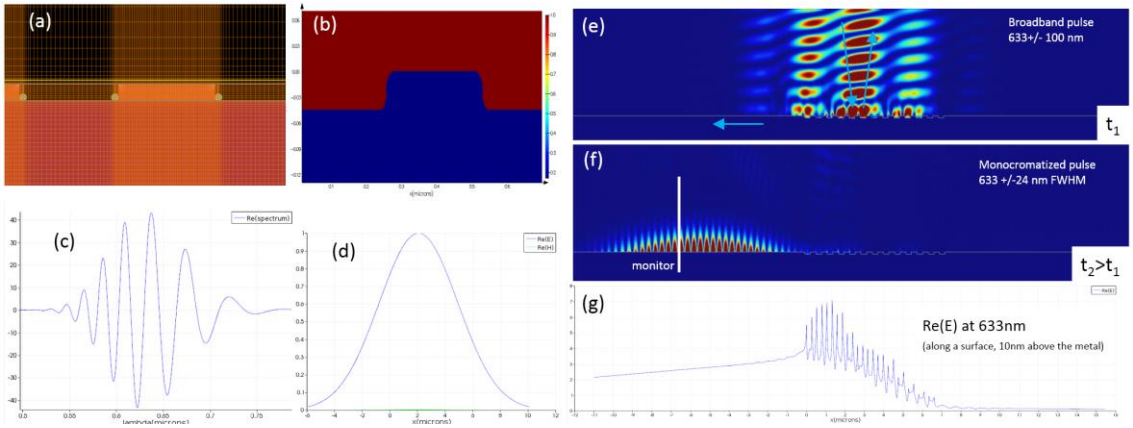

Figure S1. Electromagnetic simulation of the grating coupler. a) Detail of the adaptive mesh refinement, used for each groove tooth. b) Refractive index monitor, evidencing the round shaped corners. c) and d) temporal and spatial extension of the Gaussian pulse used for the simulation. e) and f) Electromagnetic simulation snapshots taken at consecutive time position, during the pulse illumination and during the SPP propagation along the surface. g) Real part of the electric field normal to the surface monitored 10 nm above the metal. It shows the coupling efficiency and the damping of the SPP along the surface during the propagation.

Incidentally, we note that this choice does not provide important differences to the simulation results, confirming that the launching of SPP is mainly a grating effect rather than the result of single edge coupling.

The input beam consisted of a time-domain pulse with a spectral width of +/-100 nm around 633 nm. We used perfectly matched layers as boundaries of the simulated area and the Particle Swarm Optimization (PSO) technique implemented in the FDTD commercial software as optimization routine. Although it is not possible to quantify the uncertainties corresponding to the determination of the best parameters with this PSO method, it demonstrates to be extremely effective in solving multi-parameter problems. We allowed it to span the degrees of freedom space until no sensible change in the Figure of merit was reached. Typically, we considered 100 starting configuration generation for a maximum of 120 generation steps,[4, 5] thought the convergence occurred after few tens of reiterations.

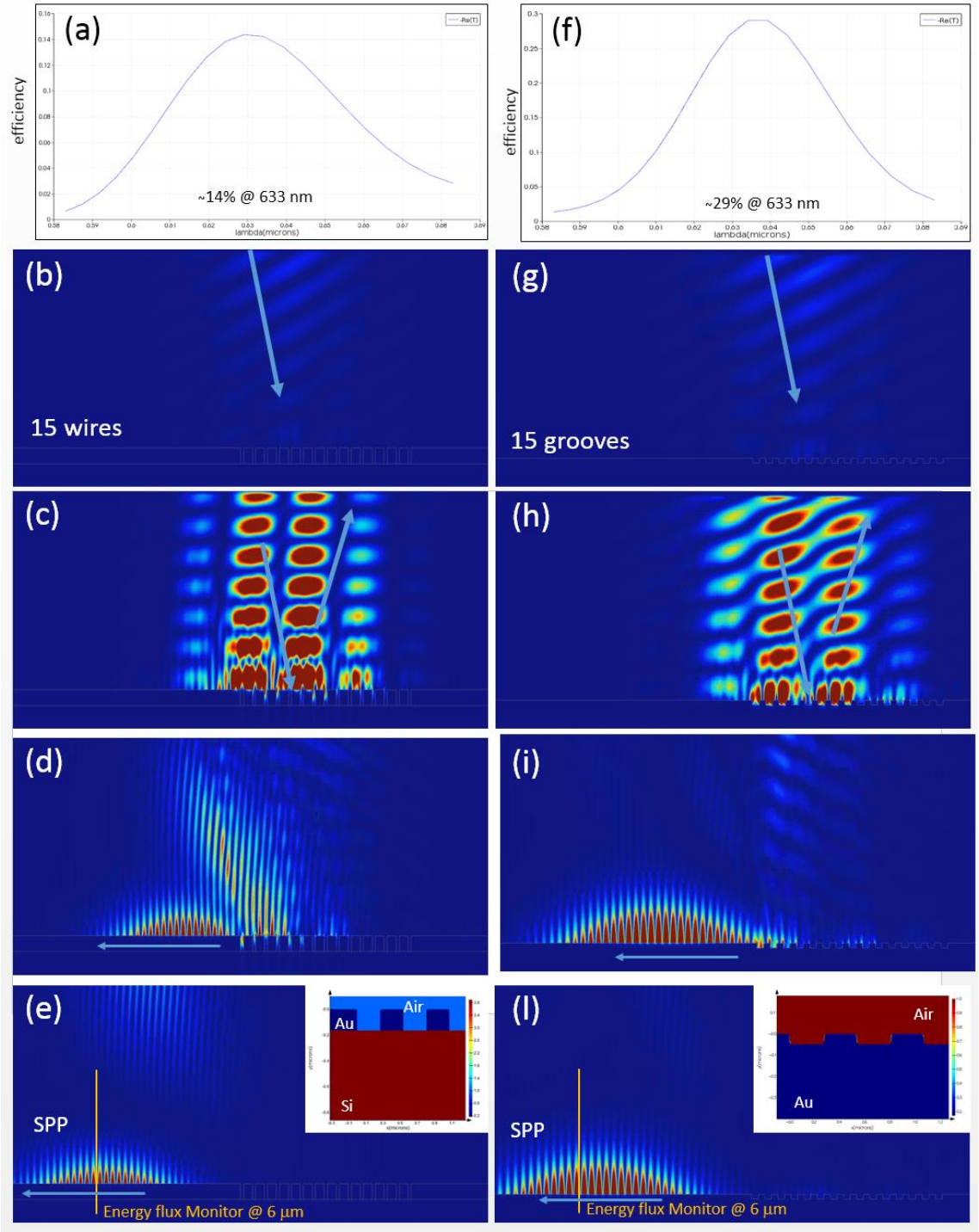

Figure S2. Electromagnetic simulation of two different kinds of grating couplers. a) to e) refer to a grating constituted by isolated Au wires deposited on the Si substrate, while f) to l) refer to a grating coupler realized on a continuous gold film. The refractive index monitors reported as insets of *F*igure S2e and S2l highlight the different kind of grating. a) and f) report the spectral normalized energy transmission trough a monitor set at 6 µm from the grating firing edge. b) to e) and g) to l) show 4 frames of the pulse propagation.

Optimization of the grating is then further improved considering the possibility to modulate the coupling/decoupling strength. In general, two strategies are adopted to produce the variable coupling rate along the grating: the modulation of the grooves depth or duty cycle. Considering the practical fabrication tolerances, we chose to modulate the grating by allowing varying the duty cycle and the pitch locally. In this way, simply adding a linear dependence to these parameters with respect to the position we get an improvement larger than 5%, as shown in Figure S3a, b. The results are in good agreement with the literature that demonstrates a similar parameter dependence.[6] We are aware that, for each scattering geometry, only a global approach for the electromagnetic field scattered by the collection of grooves can identify the optimal geometrical coupling parameters. In the cited literature case, an efficiency up to 50% was reached[6] for an Ag grating at 476 nm. There, the total launching efficiency was maximized considering as independent parameters the depth, the width and the location of each groove within an iterative scheme. This approach is particularly time-consuming considering the rapidly increasing phase space spanned by the free parameters. However, it gives the best results and proves to be the only usable for complex 3D geometries.

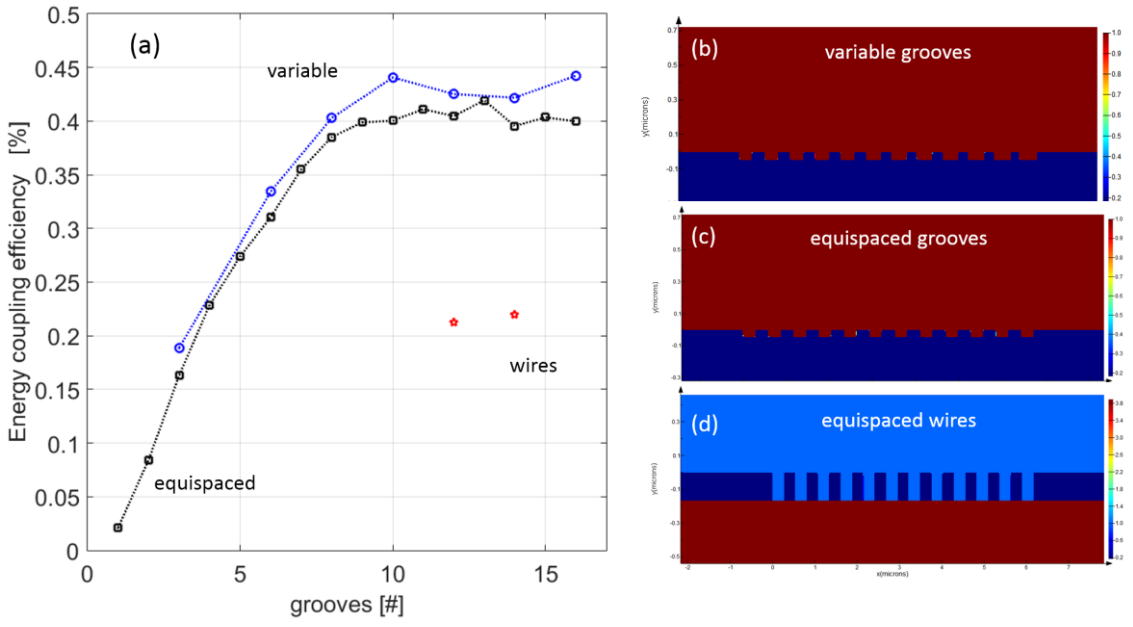

Figure S3. Energy coupling efficiency for three different kinds of grating couplers. a) Comparison of the maximal efficiency obtained at the firing edge of the gratings, simulating the same scattering geometry b), c) and d) are the refractive index monitors of the devices showing the structure of the

three different types of gratings whose simulation are reported in a). For the same scattering geometry, different arrangement of the grating profile optimizes the SPP coupling.

S2. Optical set-up, electronic scheme and measurements analysis.

To measure the local generalized photoelectric effect we have settled a setup based on an Atomic Force Microscope (AFM, MFP3D_Bio model from Asylum Research), which employs a fast high-gain current amplifying circuit and a custom optical system. We are therefore able to illuminate the tip surface and to record the current within the range 1 pA-10 μA.

The AFM is positioned upon an inverted microscope (Nikon) that allows the illumination and collection of the scattered light either with the use of fluorescence cubes or with a dedicated high-resolution optical spectrometer. The setup is shown in Figure S4 with two close-up photos of the experimental stage. In this picture, the current circuitry described in the caption of Figure S5 and the laser optical path inside the thermo- and humidity-regulated and acoustically isolated hood are visible.

We amplified the signal with a dual ORCA trans-impedance amplifier (TIA) with a current-to-voltage conversion gain up to 10^9, an amplification bandwidth of 20 kHz (-3db) and a very low current noise integrated over the whole bandwidth (<1 pA). These approaches allowed two different sensitivities of 1V/nA and 1V/μA. The sample was externally biased using an arbitrary function generator in the ±10 V range.

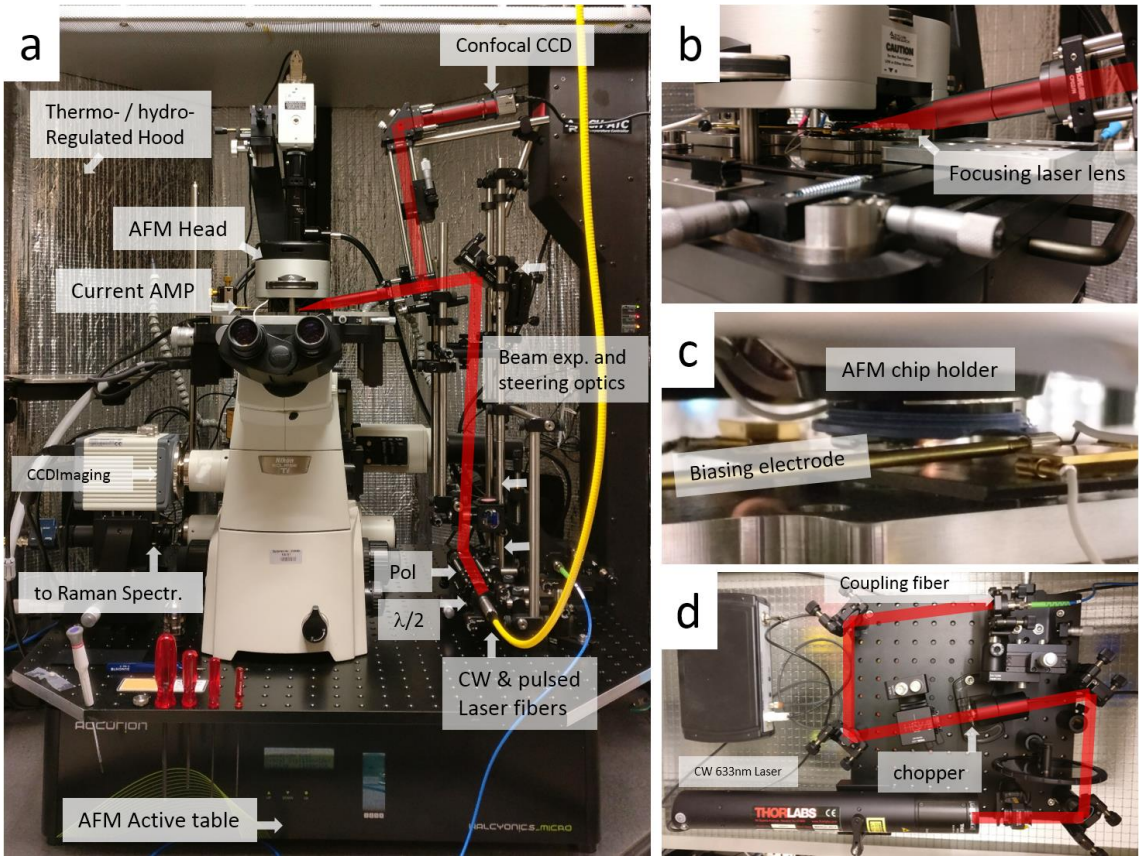

Figure S4. Photographs of the optical setup; a) photo spectroscopic AFM, are indicated the main components and the optical paths. b) and c) show the sample area where the laser and optical access and the electronic contacts are visible. d) laser optical bench; there are the beam intensity monitor and the mechanical light modulator before the coupling to the single mode fiber going to the AFM stage.

Currents were pre-filtered by a Stanford Research filtering unit, applying a 6 dB/oct Bessel low-pass filter at 7-27 KHz. We used it to filter unwanted noise Figures and all other possible features in the signal at frequencies higher than the accessible bandwidth of the low noise amplifiers. However, the system still retains enough bandwidth in order to properly acquire in a significant timescales range. A 250 Msample/sec oscilloscope was used to monitor the signals routinely. Up to 6 signals (I, V_{Bias}, trigger signal, laser pulse profile and x,y,z-AFM position) were recorded using a National Instruments PXI equipped with a 24 bit PXI4462 and a PXI6366 16 bit ±10 V parallel acquisition boards at 200 KHz sampling rate.

All the measurements were performed in Tip-Sample contact (AFM contact mode). The photoexcitation was performed by single mode lasers, vertically polarized (~ along principal tip axis), at λ=633 nm (1.98 eV). To take control of biases and drift effects (slow drifts and acoustic excitations) typically affecting AFM measurements during the time measurement we modulated the laser amplitude with a square wave at a frequency of 570 Hz with a 50% duty-cycle and applied a rigid control on the measured temperature. We used a heater element regulated by a PID controller, while the humidity of the hood was regulated flushing dried air into the chamber. Measurements were performed at 29±0.25 °C and RH <10%.

For the current to voltage measurements discussed in the main text, the two characteristics with and without illumination were retrieved via a post-processing routine in Matlab®. It allowed the full analysis of the temporal waveform signals. For the electric map (discussed in the main text), the photo-induced current was obtained via a real-time demodulation of the signal with a lock-in amplifier (LIA). In particular, the reference signal was acquired from IR led-photodiode (PD) pair and used to filter out the AC part of the measured current, synchronous with the laser pulses, to finally obtain the laser induced contribution to the measured current. The current signal at the exit of the first amplifier was AC coupled by a bandpass filtering electronics (SIM 965 high pass first order Bessel filter, HP frequency =27 Hz AC coupled, SIM 965 low pass first order Bessel filter, HP frequency =7-27 kHz, DC coupled) to the external LIA (Stanford Research SR830, sensitivity 100mV, first order low pass filter) to filter out all possible contributions not synchronous with laser modulation, leaving just the laser induced component. The output signal was then time averaged with an integration time of 10-30 ms and acquired by AFM electronics, while the tip was scanned over the sample, resulting in a hot electron image acquired in parallel to sample topography. The current contribution coming from different parts of the sample were easily discriminated, as shown in Figure 5 in the main text.

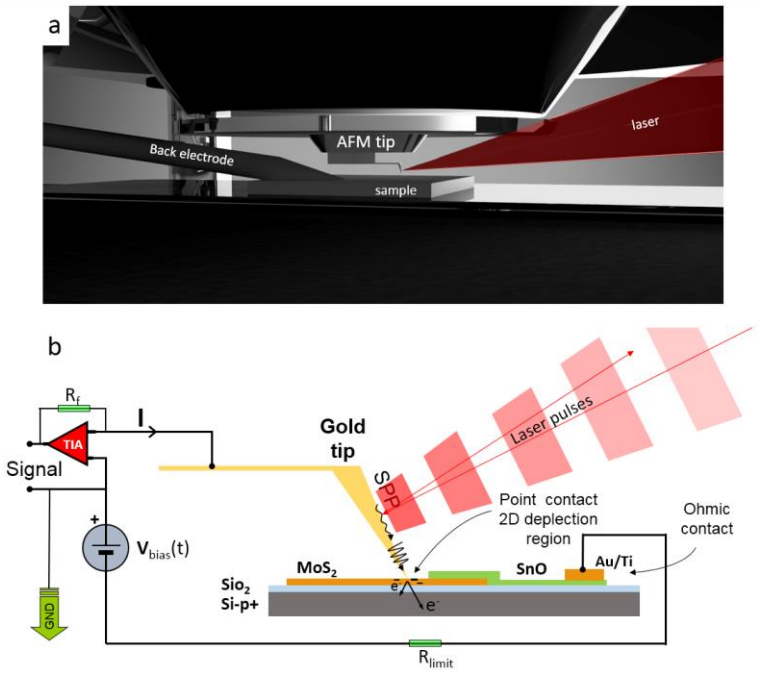

Figure S5. AFM hot carrier nanoscopy microscope. (A) Close-up rendering of the experimental AFM microscope setup used for current measurements. (B) Experimental scattering geometry and basic current circuitry scheme comprehensive of the vdW heterojunction. Photo-generated currents are read using a TIA amplifier and eventually demodulated with a LIA (not shown), then fed into the auxiliary input of the AFM driver.

S3. Band diagram of the Au-tip to heterojunction contact.

Figure S6, S7 and S8 show the energy band diagram of the metals and heterojunction involved in the experiment. Work functions, electric susceptibilities, and band gap are retrieved from literature and indicated in the captions of the Figures. The experimental Kelvin probe force microscope results, presented in the paper, have been used to evaluate the SnO susceptibility with respect to the known one of the MoS_2. In particular, for the specific sample measured, we have obtained a valued of 4.3 eV.

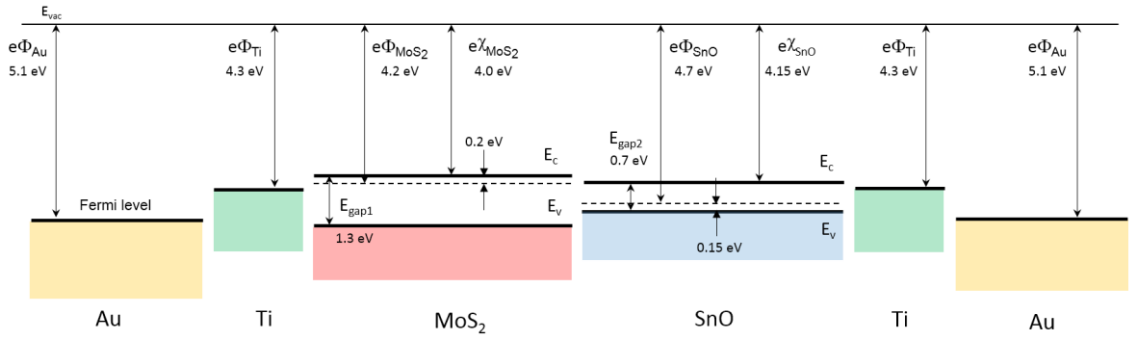

Figure S6. Flat band equilibrium diagram of the energy levels of the sample. Au, Ti, MoS_2 data from.[7] SnO susceptibility and work function derived from KPFM measures reported in this paper. SnO indirect band gap data from.[8] Optical direct band gap for the sputtered SnO sample is about 2.7 eV.[1]

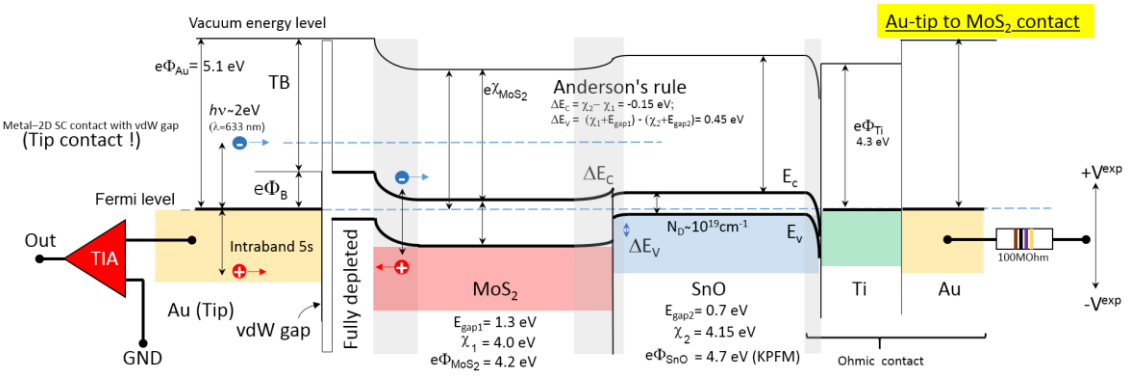

Figure S7. Expected energy band diagram for the experimental setup and basic polarization circuit scheme. Au tip in contact with the MoS_2 sample. As expected from the pure contact of Au with the top layer of the MoS_2 a vdW gap generates because the pristine surface of the 2D material does not tend to form a covalent bond. This contact is quite different from the case of pure edge contact. The fully depleted volume, characteristic of the 2D material[9] is also shown. All meaningful quantities used to design the scheme are reported.

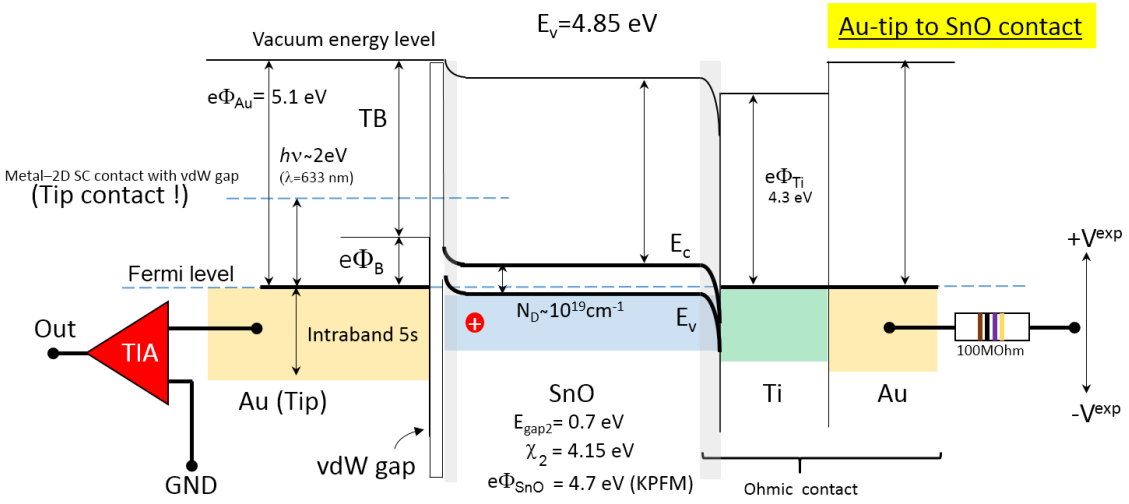

Figure S8. Expected energy band diagram for the experimental setup, for Au tip contact with the SnO sample. Not fully depleted volume is expected under the scanning tip because of the high doping level typical of this sample. It is expected to extend at most 10 nm.

S4. Raman confocal mapping analysis.

To evaluate the overall quality of the MoS_2/SnO junction and the homogeneity of the exfoliated MoS_2 layered surface we adopted Raman and photoluminescence spectroscopies that allow evaluating the vibrational and excitonic properties of the materials.

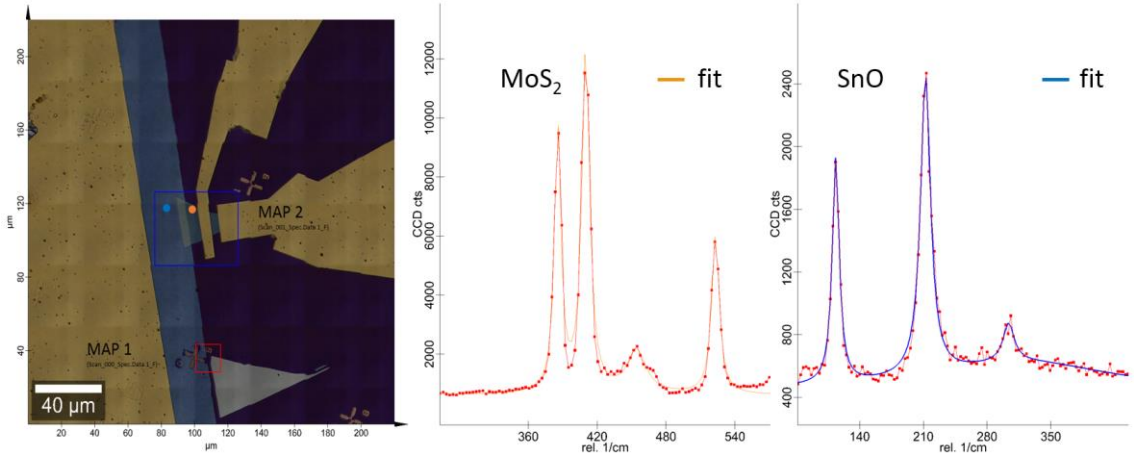

Figure S9. Optical image of the seven layers junction. On the optical image are highlighted the areas investigated with the Raman scattering and photoluminescence spectroscopies as well as the two positions about the two Raman spectra reported. Continuous lines superimposed to the collected spectra are the reconstructed profile in the interested spectral range.

A set of 150x120 spectral points mapped a 50x40 µm area, MAP2 in Figure 9. We used a f=320 mm backscattering Raman spectrometer equipped with 100X objective and excited with a linearly polarized laser at 532nm.

Each spectrum of the MAP2 was analyzed considering Lorentzian shape functions allowing the identification of the peak position, width and integrated area under the curve. In Figure 9, we show two typical Raman spectra collected from different areas of the device. The Si Raman band at 520 cm^{-1} was used as an internal frequency reference. Each spectrum was analyzed with up to seven Lorentzian curves. A background subtraction, for all materials, SnO, MoS_2, and Si, was performed on spectral data in the final fitting pass. This procedure allowed evaluating the physical quantity under the peaks with the nominal spatial resolution of 330 nm.

For each component, we have reconstructed the distribution map and obtained the corresponding statistical distribution, as shown in Figure S10 for MoS2 and Figure S11 for the SnO. The correlation graph between the components allows quantifying the homogeneity and structural quality of the sample adopting an internal reference of the spectrum.

In fact, Raman scattering spectra of the SnO material show two peaks, one at ~113 cm^{-1} and the other at ~211 cm^{-1} corresponding respectively to the Raman active modes B_{1g} and A_{1g}, that arise from different crystalline symmetries. It is thus possible to estimate the grain size, and the quality of the sputtered SnO material analyzing the map obtained as A_{1g}/B_{lg} areas ratio.

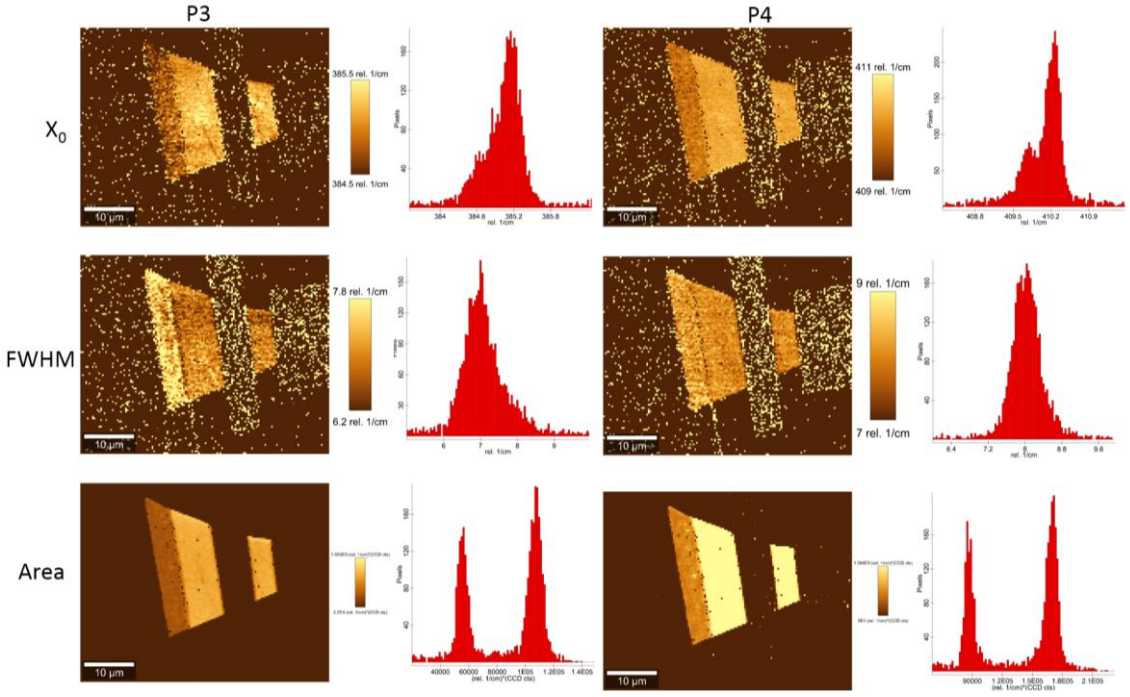

Figure S10. Raman analysis results. Here we report the position (X_0), the width (FWHM), and the integrated area (Area) under the fitted Lorentzian curves of the experimental peak, and the area, for each of the 150x120 point mapped corresponding to the two main peak of the MoS_2 7 layers flake, at nominally 385 and 410 cm^{-1}. Randomly scattered points on the images for X_0 and FWHM refer to locations where the peaks area is zero, and the corresponding parameter values during the automatic fitting procedure were missing.

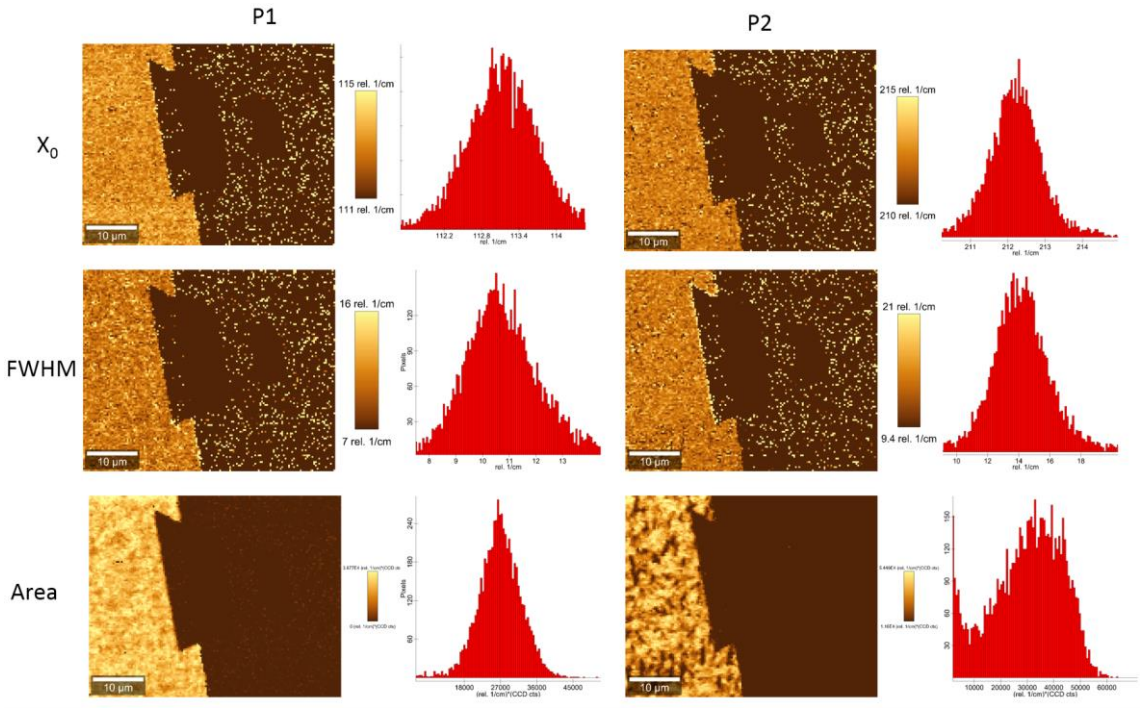

Figure S11. Raman analysis results. Here we report the position (X_0), the width (FWHM), and the integrated area (Area) under the fitted Lorentzian curves of the experimental peak, and the area, for each of the 150x120 point mapped corresponding to the two main peak of the sputtered SnO contact, nominally at 113 and 211 cm^{-1}. Randomly scattered points on the images for X_0 and FWHM refer to locations where the peaks area is zero and the corresponding parameter values during the automatic fitting procedure were missing.

S5. Supplementary current mapping.

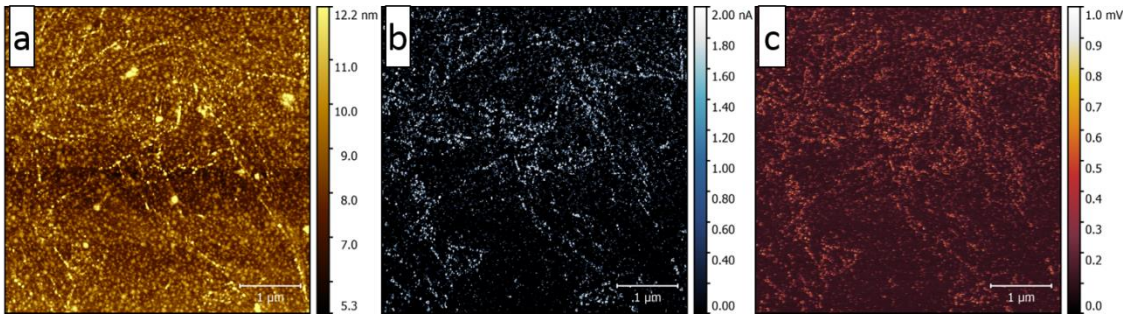

Figure S12. SnO maps: a) Topography b) total current and c) lock-in filtered signal. Showing a complete correlation between the photo-induced current and the total one in correspondence of the grain borders.

References

[1] J. A. Caraveo-Frescas, P. K. Nayak, H. A. Al-Jawhari, D. B. Granato, U. Schwingenschlögl, H. N. Alshareef, *ACS nano* **2013**, 7, 5160.

[2] Z. Wang, X. He, X.-X. Zhang, H. N. Alshareef, *Adv. Mater.* **2016**, 28, 9133.

[3] T. Tamir, S. T. Peng, *Appl. Phys.* **1977**, 14, 235.

[4] Y. Zhang, S. Wang, G. Ji, *Math. Probl. Eng.* **2015**, 2015, 38.

[5] Q. Yuan, G. Yin, *IEEE Trans. Autom. Control* **2015**, 60, 1760.

[6] J. Lu, C. Petre, E. Yablonovitch, J. Conway, *J. Opt. Soc. Am. B* **2007**, 24, 2268.

[7] H. M. Li, D. Y. Lee, M. S. Choi, D. Qu, X. Liu, C. H. Ra, W. J. Yoo, *Sci. Rep.* **2014**, 4, 4041.

[8] Y. Ogo, H. Hiramatsu, K. Nomura, H. Yanagi, T. Kamiya, M. Hirano, H. Hosono, *Appl. Phys. Lett.* **2008**, 93, 032113.

[9] A. Allain, J. Kang, K. Banerjee, A. Kis, *Nat. Mater.* **2015**, 14, 1195.